ACS APPLIED MATERIALS & INTERFACES

www.acsami.org

Research Article

Near-Infrared Photo-controlled Permeability of a Biomimetic Polymersome with Sustained Drug Release and Efficient Tumor Therapy

Yuling He, Shuwen Guo, Yue Zhang, Ying Liu,* and Huangxian Ju

Cite This: *ACS Appl. Mater. Interfaces* 2021, 13, 14951−14963

Read Online

ACCESS | Metrics & More | Article Recommendations | Supporting Information

ABSTRACT: Synthetic polymersomes have structure similarity to biovesicles and could disassemble in response to stimuli for "on-demand" release of encapsulated cargos. Though widely applied as a drug delivery carrier, the burst release mode with structure complete destruction is usually taken for most responsive polymersomes, which would shorten the effective drug reaction time and impair the therapeutic effect. Inspired by the cell organelles' communication mode via regulating membrane permeability for transportation control, we highlight here a biomimetic polymersome with sustained drug release over a specific period of time via near-infrared (NIR) pre-activation. The polymersome is prepared by the self-assembling amphiphilic diblock copolymer *P*(OEGMA-*co*-EoS)-*b*-PNBOC and encapsulates the hypoxia-activated prodrug AQ4N and upconversion nanoparticle (PEG-UCNP) in its hydrophilic centric cavity. Thirty minutes of NIR pre-activation triggers cross-linking of NBOC and converts the permeability of the polymersome with sustained AQ4N release until 24 h after the NIR pre-activation. The photosensitizer EoS is activated and aggravates environmental hypoxic conditions during a sustained drug release period to boost the AQ4N therapeutic effect. The combination of sustained drug release with concurrent hypoxia intensification results in a highly efficient tumor therapeutic effect both intracellularly and *in vivo*. This biomimetic polymersome will provide an effective and universal tumor therapeutic approach.

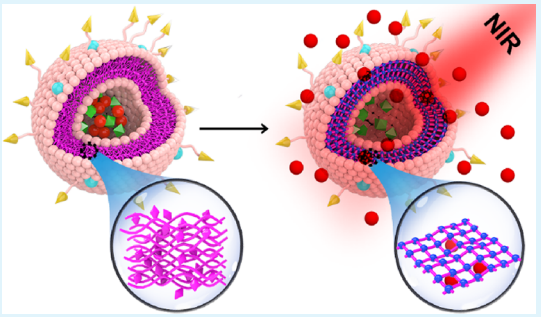

KEYWORDS: *biomimetic polymersome, NIR light, upconversion nanoparticle, sustained drug release, tumor therapy*

INTRODUCTION

Synthetic amphiphiles have biolipid-like structures and can self-assemble into polymersomes in aqueous solutions with structures like naturally originated vesicles.[1,2] Compared with liposomes, the mechanical robustness and convenience of functionalization[3−5] increase polymersome stability during the delivery process and improve targeting with controlled release, therefore making them particularly appealing as biomimetic nanocarriers and nanoreactors.[6−8] By endowing them with responsiveness toward stimuli such as specific biomarkers[9−11] and microenvironments,[12−15] "on-demand" drug delivery has been achieved. However, the complete disruption of the polymersome structure results in the uncontrolled burst release mode.[16−18] This could not maintain the drug release profile over a long period of time,[19−21] therefore requiring frequent dosing[22] or resulting in a multidrug resistance (MDR) effect[23,24] and impairing the therapeutic effect.

Different from complete structure dissociation, the cell organelles exchange specific biomolecules and support intracellular communication through tuning the permeability of their dynamic bilayer phospholipid membranes.[25,26] Permeable nanoshells with subnanometer pores could provide reaction control and selective transport via keeping the membrane structure's integrity.[18,27] As an attractive trigger for permeability control, light provides spatio-temporal precision.[28−30] Polymersome membranes equipped with azobenzene turned permeable due to the photo-triggered isomerization upon exposure to NIR[19,31−34] and X-ray[18] with sustained diffusion of payloads. However, constant light irradiation was required during the performance period over hours; otherwise, the system slowly reversed to the original impermeable state and suppressed drug release.[35] Constant NIR light irradiation is inconvenient and hazardous, therefore the capability of sustained drug release in response to NIR irradiation pre-activation is highly desired.

Taking advantage of the photo-triggered cross-linking reaction, here we fabricate a biomimetic polymersome with a sustained drug release over a long period of time via NIR pre-

Received: January 13, 2021
Accepted: March 18, 2021
Published: March 25, 2021

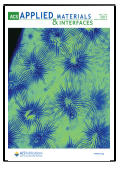

https://doi.org/10.1021/acsami.1c00842
ACS Appl. Mater. Interfaces 2021, 13, 14951−14963

activation. The amphiphilic diblock copolymer *P*(OEGMA-*co*-EoS)-*b*-PNBOC (POPN) is synthesized via reversible addition−fragmentation chain transfer (RAFT) polymerization of the hydrophobic monomer NBOC and hydrophilic block *P*(OEGMA-*co*-EoS) (Scheme 1a) and self-assembles via a hydrophobic−hydrophobic interaction into a biomimetic polymersome with a vesicle-like structure of the bilayer membrane and aqueous solution-filled centric cavity. The hydrophobic block PNBOC that stacks together as the polymersome membrane contains a photo-labile functional group, 2-nitrobenzyl, which liberates 2-nitrobenzaldehyde and CO_2 upon UV irradiation and leaves the primary amine in PNBOC.[15] The freshly generated primary amine immediately cross-links with the ester group from the neighboring PNBOC through amidation reaction, leading to the hydrophobic-to-hydrophilic transition of the polymersome membrane with the corresponding conversion of the polymersome from impermeable to permeable. Water-dispersed upconversion nanoparticles with the PEG ligand (PEG-UCNPs) are encapsulated in the centric cavity of the polymersome, which convert NIR irradiation to UV emission to achieve permeability of the polymersome. The hydrophilic prodrug AQ4N, as the model drug, is also encapsulated in the centric cavity of the polymersome with PEG-UCNPs to demonstrate the sustained drug release from polymersome (Scheme 1b).

Scheme 1. Schematic Illustration of (a) Composition of the Amphiphilic Diblock Copolymer POPN, (b) AQ4N/PEG-UCNPs-Polymersome Assembly with Permeability Conversion, and (c) Its Intracellular Delivery and Mitochondrion Location with NIR Pre-activated Sustained AQ4N Release and Singlet Oxygen Generation

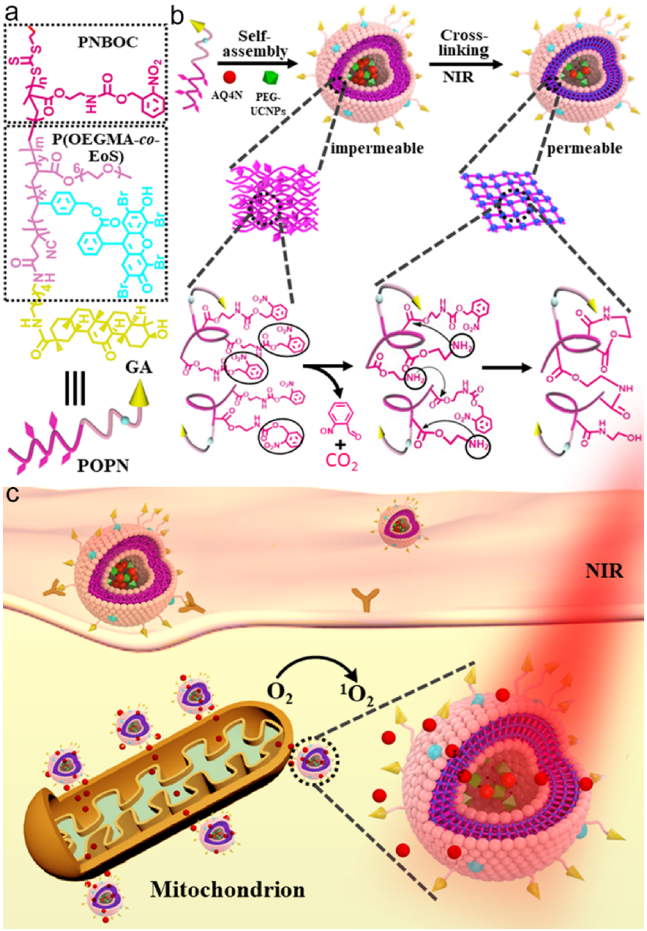

The as-prepared polymersome is further functionalized with glycyrrhetinic acid (GA) to facilitate intracellular delivery and locate it in proximity to the mitochondrion. Upon NIR pre-activation for 30 min, the polymersome membrane gradually converts from impermeable to permeable while its structure retains its integrity, which results in the sustained release of the encapsulated AQ4N in a steady manner up to 24 h. Meanwhile, the photosensitizer eosin Y contained in the hydrophilic block *P*(OEGMA-*co*-EoS) is also activated by another emission of PEG-UCNPs at 526/544 nm. Taking advantage of the oxygen supply from the mitochondrion, the polymersome also demonstrates effective conversion of molecular oxygen ($^3O_2$) to singlet oxygen ($^1O_2$), which consumes microenvironment oxygen and damages tumor vasculatures to further aggravate the tumor hypoxic situation to boost the effect of the hypoxia-activated prodrug AQ4N (Scheme 1c). Owing to the sustained release mode with NIR irradiation pre-activation, the AQ4N action period matches with the hypoxia intensification duration, which effectively enhances its therapeutic efficiency. This biomimetic polymersome with permeability transition upon NIR pre-activation provides a universal and robust fashion for sustained drug release and would benefit cancer therapy.

RESULTS AND DISCUSSION

Synthesis and Characterization of the PEG-UCNPs-Polymersome. Oligo(ethylene glycol) monomethyl ether methacrylate (OEGMA) was mixed with synthetically derived eosin Y (derived EoS) (Figure S1a) to synthesize the hydrophilic block $P(OEGMA_{0.98}\text{-}co\text{-}EoS_{0.02})_{11}$ (Figure S2a) via RAFT polymerization with 4-cyano-4-(propylsulfanylthiocarbonyl)sulfanyl pentanoic acid (ECT) (Figure S1b) as an RAFT agent.[36] The hydrophobic monomer 2-nitrobenzyloxycarbonylaminoethylmethacrylate (NBOC) was synthesized (Figure S1c) and reacted together with the above obtained hydrophilic block $P(OEGMA_{0.98}\text{-}co\text{-}EoS_{0.02})_{11}$ to synthesize the amphiphilic diblock copolymer POPN via RAFT polymerization (Figure S2b). Considering the effect of the hydrophobic chain length on the morphology of the self-assembled nanostructure, the DP (polymerization degree) for the hydrophobic block PNBOC in POPN was optimized among 18, 37, 46, and 53, and the corresponding structural parameters are listed in Table S1. The as-synthesized amphiphilic diblock copolymers POPN (P1−P4) were dispersed in THF and self-assembled, respectively, via a hydrophobic−hydrophobic interaction upon the addition of water to generate biomimetic nanostructures. P1 had the short length of PNBOC with a lower DP of 18 and self-assembled into a micelle structure with a diameter of 22 ± 3.1 nm (Figure 1a), while P2−P4 had the longer length of PNBOC with a higher DP and self-assembled into biomimetic vesicle-like structures with diameters of 34 ± 4.2, 190 ± 4.7, and 530 ± 24.6 nm, respectively (Figure 1b−d). The corresponding hydrodynamic diameters of the self-assembled nanostructures from P1−P4 were 43 ± 3.0, 64 ± 4.4, 220 ± 3.8, and 587 ± 13.9 nm, respectively, by dynamic light scattering (DLS) measurements (Figure S3). The self-assembled diblock copolymer P3 $P(OEGMA_{0.98}\text{-}co\text{-}EoS_{0.02})_{11}\text{-}b\text{-}PNBOC_{46}$ with a membrane thickness of 16 ± 3.3 nm demonstrated an appropriate size for *in vivo* delivery with an extended

https://doi.org/10.1021/acsami.1c00842
ACS Appl. Mater. Interfaces 2021, 13, 14951−14963

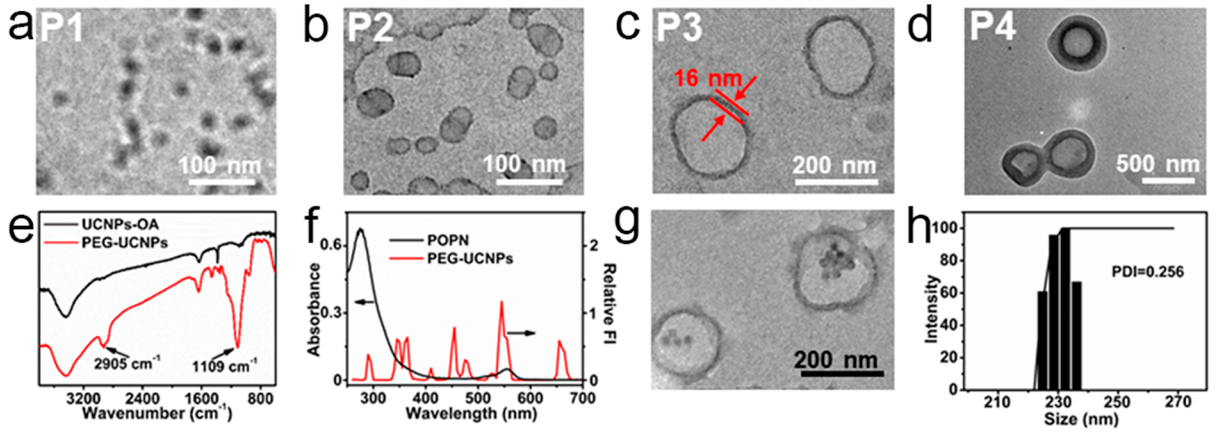

Figure 1. (a–d) TEM images of the self-assembled nanostructures composed of $P(OEGMA_{0.98}\text{-}co\text{-}EoS_{0.02})_{11}\text{-}b\text{-}PNBOC_{18}$ (P1), $P(OEGMA_{0.98}\text{-}co\text{-}EoS_{0.02})_{11}\text{-}b\text{-}PNBOC_{37}$ (P2), $P(OEGMA_{0.98}\text{-}co\text{-}EoS_{0.02})_{11}\text{-}b\text{-}PNBOC_{46}$ (P3), and $P(OEGMA_{0.98}\text{-}co\text{-}EoS_{0.02})_{11}\text{-}b\text{-}PNBOC_{53}$ (P4). (e) FT-IR spectra of oleic acid-stabilized UCNPs (UCNPs-OA) and PEG-UCNPs. (f) Upconversion luminescence spectra of PEG-UCNPs and UV–vis absorption spectra of POPN. (g) TEM image and (h) DLS analysis of the PEG-UCNPs-polymersome.

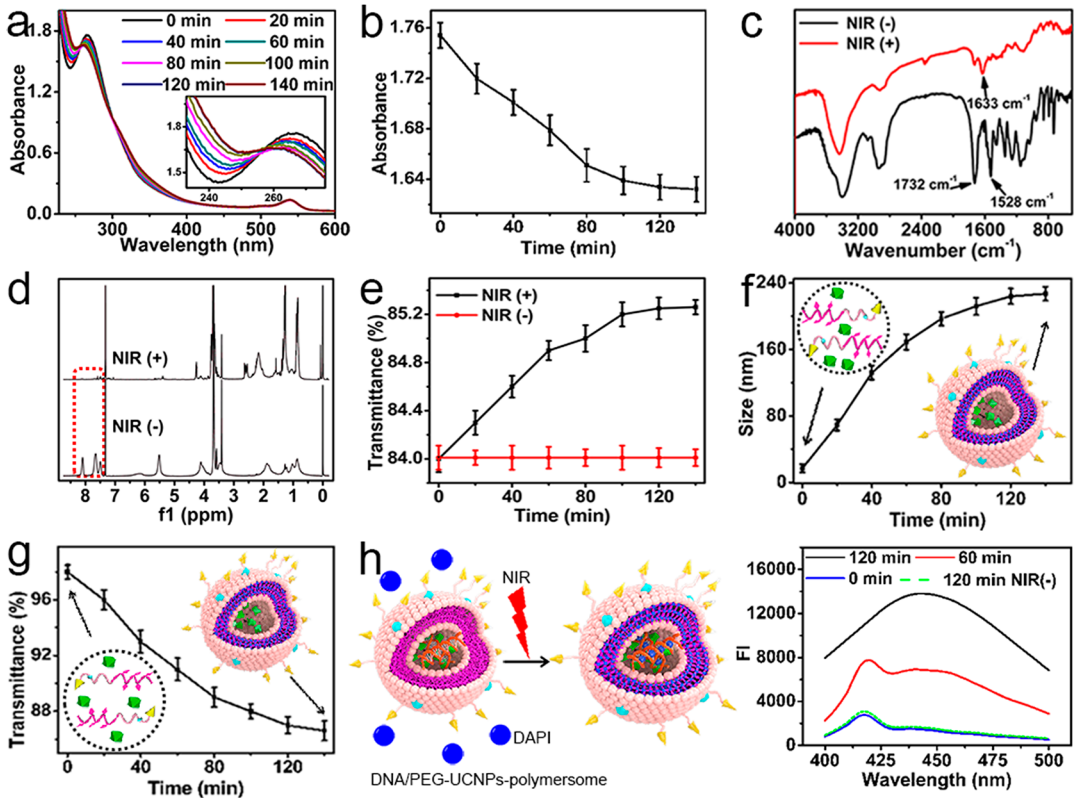

Figure 2. (a) UV–Vis absorption spectra of the PEG-UCNPs-polymersome and (b) its absorbance intensity at 280 nm in response to different NIR exposure times (the inset for (a) is the absorbance between 230 and 285 nm). (c) FT-IR spectra of the PEG-UCNPs-polymersome before (NIR(−)) and after NIR irradiation (NIR(+)). (d) ^{1}H NMR spectra recorded for the PEG-UCNPs-polymersome before (NIR(−)) and after NIR irradiation (NIR(+)) ($CDCl_3$, 400 MHz). (e) Optical transmittance of the PEG-UCNPs-polymersome at 700 nm in PBS (pH 7.4) according to time in the presence (NIR(+)) and absence (NIR(−)) of NIR irradiation. (f) DLS analysis and (g) optical transmittance of the THF-dispersed PEG-UCNPs-polymersome after different times of NIR irradiation. (h) Schematic illustration and fluorescence spectra of the DAPI and DNA/PEG-UCNP-encapsulated polymersome mixture solution in the 60 and 120 min NIR irradiation (60 min, 120 min) and in the absence of NIR irradiation (0 min, 120 min NIR(−)). The data error bars in (b), (e), (f), and (g) indicate means ± SD (n = 5).

circulation time and enhanced accumulation in cancer sites[37] and a high loading capacity, thus this was chosen as the biomimetic polymersome for therapy (Figure 1c and Figure S3, P3).

Tm^{3+} (2%), Er^{3+} (0.2%), Gd^{3+} (10%), and Yb^{3+} (20%) co-doped upconversion nanoparticles (UCNPs ($NaYF_4$:Yb,Gd,Tm,Er)) were synthesized according to a previously reported solvent thermal method, and the doped Gd^{3+} shrank the particle size.[38] The surface ligand oleic acid (OA) was then exchanged with synthesized PEG-POOH to obtain PEG-stabilized UCNPs (PEG-UCNPs) that well dispersed in aqueous solution. The ligand exchange process increased UCNPs' particle size from 13 ± 1.0 nm (oleic acid-stabilized UCNPs) to 16 ± 1.3 nm (PEG-UCNPs), while the

https://doi.org/10.1021/acsami.1c00842
ACS Appl. Mater. Interfaces 2021, 13, 14951−14963

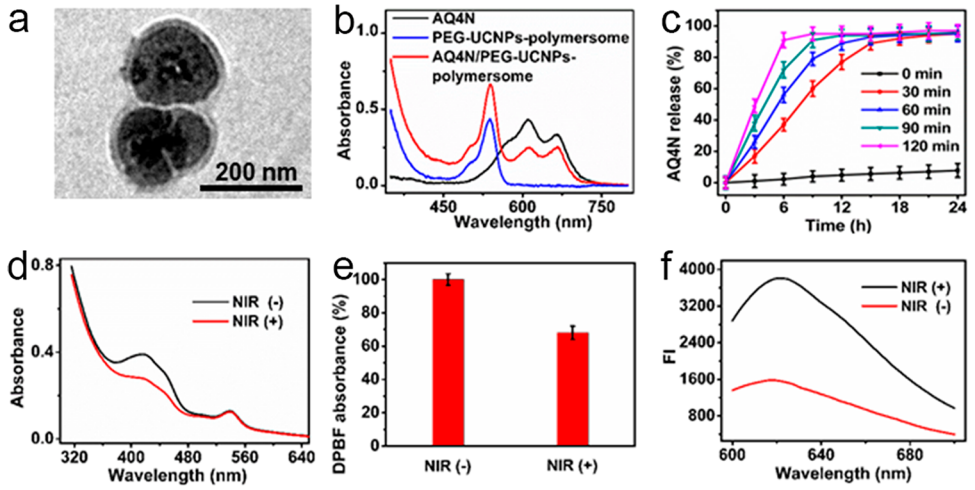

Figure 3. (a) TEM images of the AQ4N/PEG-UCNPs-polymersome. (b) UV−Vis absorption spectra of the AQ4N, PEG-UCNPs-polymersome, and AQ4N/PEG-UCNPs-polymersome. (c) Release efficiency of AQ4N from the AQ4N/PEG-UCNPs-polymersome in the absence and presence of different time NIR irradiations. (d) UV−Vis absorption spectra and (e) relative DPBF absorbance at 422 nm for the PEG-UCNPs-polymersome solution in the absence (NIR(−)) and presence (NIR(+)) of a 30 min NIR irradiation. (f) Fluorescence spectra of $[Ru(dpp)_3]Cl_2$ in the PEG-UCNPs-polymersome solution in the absence (NIR(−)) and presence (NIR(+)) of a 30 min NIR irradiation. The data error bars in (c) indicate means ± SD (n = 5).

hydrodynamic diameter increased from 15 ± 1.3 (oleic acid-stabilized UCNPs) to 19 ± 1.8 nm (PEG-UCNPs) (Figure S4). Compared with oleic acid-stabilized UCNPs, PEG-UCNPs demonstrated characteristic absorbance peaks at 2905 and 1109 cm^{-1} for the C−H vibration and C−O−C vibration of PEG, respectively, indicating the successful functionalization of UCNPs with the PEG ligand (Figure 1e). Upon a 980 nm excitation, the obtained PEG-UCNPs showed upconversion emission peaks at 290, 345, and 363 nm corresponding to $^1I_6 \rightarrow {}^3H_6$, $^1I_6 \rightarrow {}^3F_4$, and $^1D_2 \rightarrow {}^3H_6$ transitions of Tm^{3+}; 455 and 475 nm corresponding to $^1D_2 \rightarrow {}^3F_4$ and $^1G_4 \rightarrow {}^3H_6$ transitions of Tm^{3+}; 411, 526, and 544 nm corresponding to $^2H_{9/2} \rightarrow {}^4I_{15/2}$, $^2H_{11/2} \rightarrow {}^4I_{15/2}$, and $^4S_{3/2} \rightarrow {}^4I_{15/2}$ transitions of Er^{3+}; and 650 nm corresponding to $^4F_{9/2} \rightarrow {}^4I_{15/2}$ transitions of Er^{3+} (Figure 1f), respectively. After that, the nontoxic PEG-UCNPs were encapsulated into the interior aqueous cavity of the polymersome during the diblock copolymer POPN self-assembly process. The PEG-UCNP-encapsulated polymersome (PEG-UCNPs-polymersome) maintained its original morphology with the particle size increased to 205 ± 4.6 nm (Figure 1g). DLS measurements showed a hydrodynamic diameter of 230 ± 3.8 nm (Figure 1h) with a polydispersity index (PDI) of 0.256, indicating a relatively uniform size distribution.

POPN demonstrated a broad absorbance at 250−387 nm due to the 2-nitrobenzyl functional group contained in the hydrophobic monomer NBOC (Figure 1f). 2-Nitrobenzyl is labile to UV irradiation and falls from nontoxic NBOC with the generation of the primary amine group. In the POPN self-assembled polymersome, the freshly generated primary amine cross-linked with the ester group from the neighboring NBOC, leading to the hydrophobic-to-hydrophilic transition of PNBOC with the corresponding transition of the polymersome from impermeable to permeable (Scheme 1b). To demonstrate the UV-responsive degradation of the 2-nitrobenzyl group, POPN was exposed under a 360 nm irradiation for 10 min and showed an obvious decrease for the 2-nitrobenzyl characteristic absorbance peak at 280 nm (Figure S5).

NIR Photo-Controlled Membrane Cross-linking for the PEG-UCNPs-Polymersome. The upconversion luminescence peaks of PEG-UCNPs at 290 and 345/363 nm upon NIR irradiation well overlapped with the characteristic absorption of POPN (Figure 1f), endowing the PEG-UCNPs-polymersome responsiveness to NIR irradiation. Upon a 980 nm irradiation, the characteristic absorption peak of NBOC at 280 nm exhibited successive decrease according to time and saturated at 100 min (Figure 2a,b), indicating the complete inter-cross-linking of NBOC. FT-IR characterization was also performed to trace the primary amine generation process and subsequent cross-linking reaction for NBOC in the PEG-UCNPs-polymersome. After NIR irradiation, $-NO_2$ characteristic absorbance peaks at 1351 and 1528 cm^{-1} for the N−O vibrations and the aromatic ring characteristic absorbance peak at 700−900 cm^{-1} for the C−H vibration disappeared (Figure 2c) accompanied by the disappearance of the aromatic ring chemistry shift at 8.1−7.4 ppm in ^1H NMR (Figure 2d), indicating the efficient cleavage of the 2-nitrobenzyl group from NBOC. Meanwhile, the −COO− characteristic absorbance peak at 1732 cm^{-1} corresponding to the C═O vibration showed a considerable decrease with an increase in the −CONH− characteristic absorbance peak at 1633 cm^{-1} corresponding to the C═O vibration (Figure 2c), indicating the efficient cross-linking of the neighboring NBOC via amidation reaction. The membrane cross-linking upon NIR irradiation enhanced the permeability of the self-assembled polymersome, thus increasing the optical transmittance of the polymersome from 84.0 to 85.2% (Figure 2e). Furthermore, the PEG-UCNPs-polymersomes with different NIR irradiation times were diluted with excess THF, which disassembled the uncross-linked PEG-UCNPs-polymersome while keeping the cross-linked PEG-UCNPs-polymersome's integrity. In the absence of NIR irradiation, the PEG-UCNPs-polymersome was completely disassembled in THF with a hydrodynamic diameter of 20 ± 3.7 nm for dispersed PEG-UCNPs (Figure 2f) and an optical transmittance of ∼98% (Figure 2g). With the extended NIR irradiation time, the hydrodynamic diameter of the THF-dispersed PEG-UCNPs-

https://doi.org/10.1021/acsami.1c00842
ACS Appl. Mater. Interfaces 2021, 13, 14951−14963

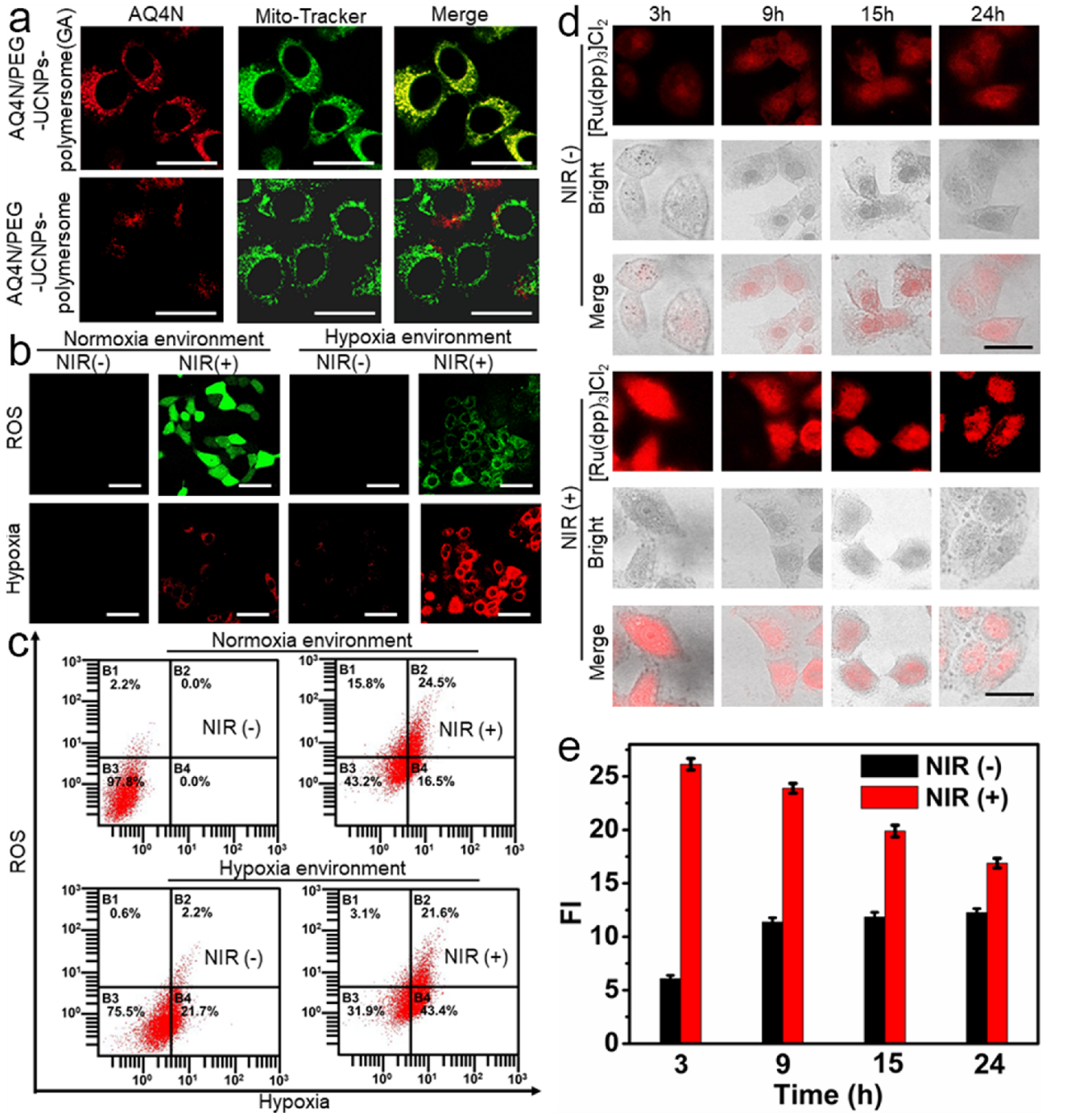

Figure 4. (a) Confocal fluorescence images of mitochondrial co-localization of the AQ4N/PEG-UCNPs-polymersome(GA) and AQ4N/PEG-UCNPs-polymersome (scale bar: 20 μm). (b) Confocal fluorescence images of PEG-UCNPs-polymersome(GA)-treated HepG2 cells incubated with an ROS/hypoxia detection kit in normoxic/hypoxic environments with the presence/absence of NIR light irradiation (scale bar: 50 μm). (c) ROS and hypoxia generation measurements via flow cytometry analysis for AQ4N/PEG-UCNPs-polymersome(GA)-treated HepG2 cells in normoxic/hypoxic environments with the presence and absence of NIR irradiation (2 W/cm^2). (d) Time-dependent confocal fluorescence images of PEG-UCNPs-polymersome(GA)-treated HepG2 cells in a hypoxia incubator (5% O_2) in the presence and absence of NIR irradiation (2 W/cm^2). $[Ru(dpp)_3]Cl_2$ fluorescence was recorded in a λex/em of 488/600−700 nm (scale bars: 20 μm). (e) Semiquantitative analysis of $[Ru(dpp)_3]Cl_2$ fluorescence intensity (d) using Image-Pro Plus 6.0 software. The data error bars in (e) indicate means ± SD (n = 5).

polymersome linearly increased and saturated at 232 ± 4.9 nm with a 120 min NIR irradiation (Figure 2f), and the optical transmittance in THF decreased to 86.8% (Figure 2g). These results indicated the successful POPN cross-linking upon NIR irradiation and the corresponding formation of the rigid and permeable polymersome structure. To confirm the effect of polymersome permeability on molecule passage, the dye 4,6-diamidino-2-phenylindole (DAPI) was mixed with the DNA/PEG-UCNP-encapsulated polymersome and showed a strong DAPI fluorescence at 420 nm. After NIR irradiation, the permeability transition of the polymersome allowed DAPI to diffuse into the aqueous cavity of the polymersome and to embed into the polymersome-encapsulated DNA strands, which resulted in the gradual shift of the characteristic

https://doi.org/10.1021/acsami.1c00842
ACS Appl. Mater. Interfaces 2021, 13, 14951−14963

fluorescence peak to 440 nm.[39] In the absence of NIR irradiation, incubation of DAPI and the DNA/PEG-UCNP-encapsulated polymersome for 120 min did not cause a fluorescence peak shift, confirming the impermeability of the polymersome in the absence of NIR irradiation (Figure 2h).

Hypoxia-Activated Prodrug AQ4N Loading in the Polymersome with NIR-Controlled Sustained Release and Hypoxia Generation. AQ4N, a hypoxia-activated prodrug that displays high toxicity selectively to hypoxic environment,[40] was loaded into the aqueous cavity of the polymersome with PEG-UCNPs during the POPN self-assembly process (AQ4N/PEG-UCNPs-polymersome). The successful encapsulation of AQ4N showed a dark polymersome interior cavity with a particle size of 209 ± 2.9 nm for the TEM image (Figure 3a) and a hydrodynamic diameter of 234 ± 2.5 nm with a PDI of 0.216 (Figure S6a) for DLS measurement, similar to that of the PEG-UCNPs-polymersome (Figure 1g,h). Compared with the PEG-UCNPs-polymersome, the AQ4N/PEG-UCNPs-polymersome showed a characteristic absorbance peak of AQ4N at 633 nm (Figure 3b). The loading efficiency and loading capacity of AQ4N in the PEG-UCNPs-polymersome were, respectively, calculated as 98 (w/w) and 49% (w/w) by comparing the absorbance of the AQ4N/PEG-UCNPs-polymersome at 633 nm with the AQ4N absorbance standard calibration curve (Figure S6b), which was comparable to that of the previously reported loading capacity.[41] Upon NIR light irradiation-induced permeability conversion of the polymersome, the encapsulated pro-drug AQ4N diffused across the polymersome membrane with a sustained release fashion. AQ4N release rates depended on the polymersome cross-linking efficiency with different NIR irradiation times. An NIR pre-activation time of 30 min resulted in sustained AQ4N release, and the release percentage reached 92 ± 2.6% at 21 h. Sixty minutes of NIR pre-activation accelerated the AQ4N release rate, and the release percentage reached 93 ± 2.8% at 15 h. A fast release was achieved with 90 and 120 min NIR light irradiations, and the release percentages reached 91 ± 2.7% in 8 h and 91 ± 2.8% in 6 h, respectively (Figure 3c). The polymersome permeability could be modulated by the NIR irradiation duration to realize the desired AQ4N release rate. The AQ4N/PEG-UCNPs-polymersome remained impermeable in the absence of NIR light irradiation, which demonstrated only a 10.2 ± 2.5% leakage within 24 h in PBS (pH 7.4) (Figure 3c), indicating the stability of the AQ4N/PEG-UCNPs-polymersome during circulation in a physiological environment. Moreover, the AQ4N/PEG-UCNPs-polymersome showed a satisfactory physiological stability upon incubation with DMEM containing 10% fatal bovine serum, which showed a stable particle size and PDI over 24 h (Figure S7).

The photosensitizer eosin Y was contained in the hydrophilic block of *P*(OEGMA-co-EoS). It is capable of generating reactive oxygen species (ROS) under 526/544 nm emissions from PEG-UCNPs encapsulated in the polymersome upon NIR irradiation. ROS generation from the PEG-UCNPs-polymersome was determined with an ROS sensing probe. 1,3-Diphenylisobenzofuran (DPBF), which reacts with ROS irreversibly to give a characteristic absorption peak at 422 nm, was incubated with the PEG-UCNPs-polymersome under 30 min of NIR irradiation and decreased its characteristic absorbance of 30% (Figure 3d,e), indicating an efficient production of ROS with NIR irradiation. O_2 in the microenvironment was consumed during the conversion of the molecular oxygen ($^3O_2$) to singlet oxygen ($^1O_2$) process[42] and boosted the effect of the hypoxia-activated prodrug AQ4N. The corresponding hypoxic condition generation upon O_2 consumption was further evaluated by incubating the PEG-UCNPs-polymersome-dispersed solution with tris(4, 7-diphenyl-1,10-phenanthroline) ruthenium(II) dichloride ($[Ru(dpp)_3]Cl_2$), an oxygen-sensitive probe, which reversibly converts between quenching and luminescence under hyperoxic and hypoxic conditions. With NIR light irradiation, $[Ru(dpp)_3]Cl_2$ demonstrated a stronger characteristic fluorescence intensity at 620 nm, indicating efficient generation of hypoxic conditions in the microenvironment (Figure 3f).

Internalization of the AQ4N/PEG-UCNPs-Polymersome and Intracellular ROS/Hypoxia Intensification. Glycyrrhetinic acid (GA), which targets protein kinase C (PKC) α overexpressed on the tumor cell membrane and interacts with the mitochondrial respiratory chain,[43] was conjugated to POPN before the polymersome self-assembly process to enhance *in vivo* delivery specificity and locate polymersomes in the vicinity to the mitochondrion. GA-mediated endocytosis was verified by confocal fluorescence images. The strong fluorescence of AQ4N was detected from AQ4N/PEG-UCNPs-polymersome(GA)-incubated HepG2 cells, while excess GA-pretreated HepG2 cells showed little fluorescence after incubation with the AQ4N/PEG-UCNPs-polymersome(GA) (Figure S8). The subsequent intracellular mitochondria targeting of the AQ4N/PEG-UCNPs-polymersome(GA) was confirmed by co-staining experiments. HepG2 cells were incubated with the AQ4N/PEG-UCNPs-polymersome(GA) and AQ4N/PEG-UCNPs-polymersome, respectively, and subsequently stained with Mito-Tracker green. The red fluorescence of AQ4N was well overlapped with green fluorescence of Mito-Tracker for AQ4N/PEG-UCNPs-polymersome(GA)-incubated HepG2 cells, indicating the successful location of the polymersome in the vicinity of the mitochondria (Figure 4a). In comparison, red and green fluorescences were separated for AQ4N/PEG-UCNPs-polymersome-incubated HepG2 cells.

ROS generation and corresponding local hypoxia intensification in living cells were investigated with intracellular ROS/hypoxia detection kits via confocal laser scanning microscopy (CLSM). HepG2 cells were incubated in a normoxic environment with sufficient oxygen supply and a hypoxic environment (mimic tumor microenvironment), respectively, and treated with the PEG-UCNPs-polymersome(GA) in the presence and absence of NIR light irradiation (2 W/cm^2, 30 min with a 5 min interval for every 10 min). Under NIR light irradiation, abundant ROS generation was detected from HepG2 cells in a normoxic environment (Figure 4b, ROS, normoxic environment, NIR(+)) while general ROS generation was detected from a hypoxic environment (Figure 4b, ROS, hypoxic environment, NIR(+)). The ROS generation under NIR light irradiation in a hypoxic environment further consumed oxygen and resulted in an intensive red fluorescence from the hypoxic detection probe (Figure 4b, hypoxia, hypoxic environment, NIR(+)), indicating the remarkably intensified intracellular hypoxic condition upon NIR irradiation. The intracellular ROS generation and hypoxia intensification were further quantified by flow cytometry assays, where B1 and B2 portions indicate ROS generation extent and B2 and B4 portions indicate a hypoxic extent.[42] HepG2 cells incubated with the PEG-UCNPs-polymersome(GA) under NIR light irradiation showed the ratio of ROS generation as 24.7% even

https://doi.org/10.1021/acsami.1c00842
ACS Appl. Mater. Interfaces 2021, 13, 14951−14963

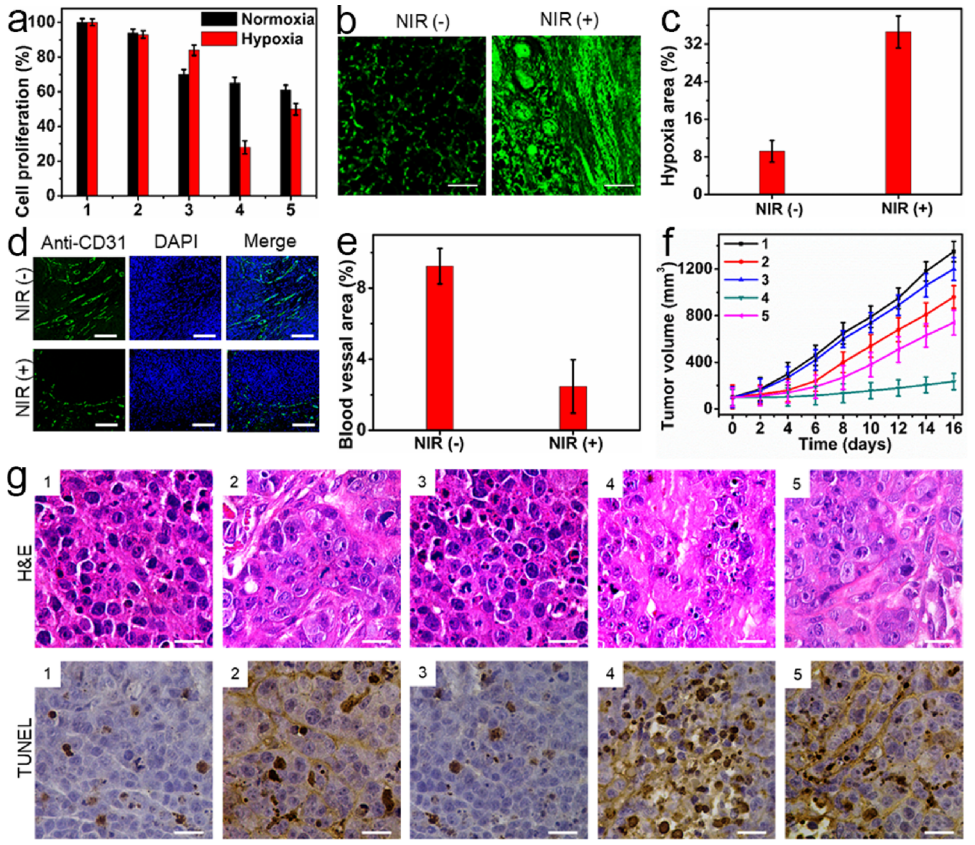

Figure 5. (a) Relative cell proliferation percentages for HepG2 cells treated with PBS, NIR(−) (1); AQ4N/PEG-UCNPs-polymersome(GA), NIR(−) (2); PEG-UCNPs-polymersome(GA), NIR(+) (3); AQ4N/PEG-UCNPs-polymersome(GA), NIR(+) (4); and mixture of the PEG-UCNPs-polymersome(GA) and free AQ4N, NIR(+) (5). The immunofluorescence images of (b) HIF-1a staining tumor slices with (c) relative hypoxic positive areas and (d) anti-CD31 staining tumor slices with (e) relative blood vessel areas from PEG-UCNPs-polymersome(GA)-treated tumor-bearing mice in the presence and absence of NIR irradiation (scale bars: 200 μm). (f) Relative tumor volume at different days and (g) histological observations of tumor tissues stained with H&E and TUNEL for HepG2 cell tumor-bearing nude mice after being treated with PBS, NIR(−) (1); AQ4N/PEG-UCNPs-polymersome(GA), NIR(−) (2); PEG-UCNPs-polymersome(GA), NIR(+) (3); AQ4N/PEG-UCNPs-polymersome(GA), NIR(+) (4); and mixture of the PEG-UCNPs-polymersome(GA) and free AQ4N, NIR(+) (5). NIR irradiation was performed with 980 nm light, 2 W/cm^2, for 30 min with a 5 min interval for every 10 min. The error bars in (a), (c), (e), and (f) indicate means ± SD (n = 5) (scale bar: 100 μm).

in a hypoxic environment, which effectively intensified intracellular hypoxic conditions from 23.9 (NIR(−)) to 65.0% (NIR(+)) (Figure 4c, hypoxic environment). The intensified hypoxic condition could be kept for a certain period of time. After the NIR irradiation of PEG-UCNPs-polymersome(GA)-treated HepG2 cells under a hypoxic environment with 5% O_2, the intracellular hypoxic condition was measured according to time using the hypoxia probe $[Ru(dpp)_3]Cl_2$. HepG2 cells showed a strong fluorescence of $[Ru(dpp)_3]Cl_2$ after NIR irradiation, demonstrating that NIR irradiation could effectively intensify intracellular hypoxic conditions. Though gradually attenuated with time, the intensification effect was able to be kept for 24 h. Despite the low $[Ru(dpp)_3]Cl_2$ fluorescence in 3 h due to the high oxygen level in cells, the hypoxic condition for PEG-UCNPs-polymersome(GA)-treated cells in the absence of NIR irradiation demonstrated unchanged levels in 24 h with constant $[Ru(dpp)_3]Cl_2$ fluorescence (Figure 4d). The semi-quantitative analysis of intracellular $[Ru(dpp)_3]Cl_2$ fluorescence also showed a higher intensity for HepG2 cells in the presence of NIR irradiation compared with that in the absence of NIR irradiation (Figure 4e). The long duration time of intensified hypoxic conditions upon a 30 min NIR irradiation overlapped with the prodrug AQ4N sustained release period, which could promote the AQ4N therapeutic effect.

Intracellular Therapeutic Effect of the AQ4N/PEG-UCNPs-Polymersome(GA) and *In Vivo* Application. The therapeutic effect of the AQ4N/PEG-UCNPs-polymersome-(GA) was evaluated with standard MTT assay, and its performance was studied in normoxic and hypoxic conditions with a 5% O_2 level (mimic tumor microenvironment).[44] The PEG-UCNPs-polymersome(GA) only demonstrated the PDT therapeutic effect under NIR irradiation due to the activation of the photosensitizer derived EoS contained in POPN. The PDT efficiency was impaired by an O_2-deficient environment (Figure 5a, column 3). The *in situ* ROS generation by NIR irradiation (2 W/cm^2, 30 min with a 5 min interval for every 10 min) intensified the intracellular hypoxic conditions, thus notably boosting the therapeutic effect of the hypoxia-activated prodrug AQ4N. The AQ4N/PEG-UCNPs-polymersome(GA) showed an impressive cell proliferation suppression of 73 ± 2.8% under NIR irradiation in a hypoxic environment, while the cell proliferation suppression was only 35 ± 2.6% under NIR light irradiation in a normoxic environment (Figure 5a, column 4). On the contrary, the AQ4N/PEG-UCNPs-polymersome(GA) barely affected cell proliferation in the

https://doi.org/10.1021/acsami.1c00842
ACS Appl. Mater. Interfaces 2021, 13, 14951−14963

absence of NIR light irradiation both in normoxic and hypoxic environments (Figure 5a, column 2) due to the impermeability of the polymersome, which prevents AQ4N release. To demonstrate the superiority of the AQ4N sustained release mode, the same amount of free AQ4N was transfected into HepG2 cells with the PEG-UCNPs-polymersome(GA) to imitate the "all-at-once" drug release mode. Though the PEG-UCNPs-polymersome(GA) kept the same hypoxia intensification effect compared with the AQ4N/PEG-UCNPs-polymersome(GA) under NIR light irradiation, the burst release of AQ4N only resulted in 50 ± 2.7% of cell proliferation suppression (Figure 5a, column 5) due to the active efflux of AQ4N by transporters like P-glycoprotein (P-gp) on the cell membrane. Flow cytometry assay results also confirmed the good therapeutic effect of the AQ4N/PEG-UCNPs-polymersome(GA), which showed the highest apoptosis rate of 66.1% for HepG2 cells with NIR light irradiation in hypoxic conditions (Figure S9, item 4). These results indicated that the impressive therapeutic effect of AQ4N for HepG2 cells was attributed to the sustained release of AQ4N triggered by NIR irradiation accompanied by a long duration time of hypoxia intensification. In addition, the AQ4N/PEG-UCNPs-polymersome(GA) demonstrated good biocompatibility with a 93 ± 3.1% cell viability even at a high concentration of 200 μg/mL (Figure S10). In addition, merely 980 nm NIR irradiation demonstrated a little effect on cell viability (Figure S11).

The *in vivo* tumor microenvironment hypoxia intensification induced by NIR irradiation (2 W/cm^2) for PEG-UCNPs-polymersome(GA)-treated mice was further evaluated by immunofluorescence staining of HIF-1a, the hypoxia-inducible factor. The tumor slices from 24 h post NIR irradiation showed bright immunofluorescence of HIF-1a compared to those without NIR irradiation (Figure 5b). The hypoxia-positive area in tumor slices was 34 ± 3.4% in the presence of NIR irradiation and 9 ± 2.3% in the absence of NIR irradiation (Figure 5c), indicating that NIR irradiation also aggravated the microenvironment hypoxic condition in tumors. The *in situ* ROS generation upon NIR irradiation not only depleted oxygen but also strongly destroyed tumor blood vessels, which would cut down tumor oxygen supply, and further aggravated tumor hypoxic conditions with a long duration time.[45] Immunofluorescence staining of anti-CD31 from tumor slices demonstrated the amount of tumor blood vasculatures 24 h post NIR irradiation. Tumor slices from the PEG-UCNPs-polymersome(GA)-treated mice group with NIR light irradiation showed a much lower fluorescence of anti-CD31 compared to those without NIR light irradiation (Figure 5d), indicating that the blood vessel area reduced from 9.5 ± 1.3% for tumor slices in the absence of NIR irradiation to 2.1 ± 1.8% for those in the presence of NIR irradiation (Figure 5e). The *in vivo* antitumor efficiency was evaluated using HepG2 cell tumor-bearing nude mice. The AQ4N/PEG-UCNPs-polymersome(GA)-injected mice with 30 min of NIR irradiation demonstrated the best inhibition for tumor growth comparing with the mouse groups treated with PBS, the AQ4N/PEG-UCNPs-polymersome(GA) in the absence of NIR light irradiation, the PEG-UCNPs-polymersome(GA) with NIR light irradiation, and the mixture of the PEG-UCNPs-polymersome(GA) and free AQ4N with NIR light irradiation (Figure 5f and Figure S12a), demonstrating the prominent *in vivo* antitumor capability of the AQ4N/PEG-UCNPs-polymersome with NIR light-activated sustained drug release. In addition, the AQ4N/PEG-UCNPs-polymersome-(GA)-treated group demonstrated the maximum necrosis of tumor cells in H&E images with the highest level of cell apoptosis in TUNEL images (Figure 5g). There was no noticeable change of mouse body weight from different groups during the treatment process (Figure S12b) and no obvious pathological abnormalities in normal organs (Figure S12c), indicating satisfactory biocompatibility and therapeutic specificity of the AQ4N/PEG-UCNPs-polymersome(GA).

CONCLUSIONS

In conclusion, the as-presented biomimetic polymersome demonstrated the capability of permeability engineering with NIR irradiation pre-activation, which resulted in sustaining drug release until 24 h and simultaneous *in vivo* hypoxic condition intensification. The combination effect showed the most efficient tumor therapy both intracellularly and in live mice. We believe that it will provide a universal and effective therapeutic approach with a sustained release mode for tumor therapy.

EXPERIMENTAL SECTION

Synthesis of Derived Eos. Eosin Y (647 mg, 1 mmol), 4-chloromethylstyrene (152 mg, 1 mmol), and K_2CO_3 (297 mg, 2.2 mmol) were dissolved in anhydrous DFM (5 mL) in a Schlenk flask under N_2 protection. After being refluxed at 80 °C for 6 h, the mixture's pressure was reduced to evaporate the solvent, and the residual solid was subsequently dissolved in dichloromethane, washed with saturated NaCl solution, dried with anhydrous $MgSO_4$, filtered, and concentrated under reduced pressure. The as-obtained crude product was purified by silica gel column chromatography with dichloromethane and ethyl acetate (v/v, from 100:1 to 10:1 as a gradient eluent). Finally, 4-vinylbenzyl 2-(2,4,5,7-tetrabromo-6-hydroxy-3-oxo-3H-xanthen-9-yl) benzoate eosin Y (derived EoS) was obtained as a red solid (663 mg, 83% yield). ^{1}H NMR (DMSO-d_6, 400 MHz, 298 K) δ (ppm): 8.22 (d, 1H, Ar-H, J = 7.79 Hz), 7.90 (m, 2H, Ar-H), 7.48 (d, 1H, Ar-H, J = 7.51 Hz), 7.25 (d, 2H, Ar-H, J = 8.19 Hz), 6.92 (s, 1H, Ar-H), 6.72 (d, 2H, Ar-H, J = 8.21 Hz), 6.65 (m, 1H, −CHCH$_2$), 5.77 (d, 1H, −CHCHH, J = 17.87 Hz), 5.28 (d, 1H, −CHCHH, J = 10.88 Hz), 5.00 (s, 2H, −COO−CH$_2$−) (Figure S1a).

Synthesis of ECT. 4-Cyano-4-(propanesulfanylthiocarbonyl)-sulfanyl pentanoic acid (ECT) as an RAFT agent was synthesized according to the previous report.[46] Sodium hydride (60% in oil) (3.15 g, 79 mmol) was dispersed in diethyl ether (150 mL). 1-Propanethiol (5.787 g, 76 mmol) was then added in over 10 min via stirring at 0 °C. Accompanied by hydrogen production, the grayish sodium hydride was transformed to white slurry of sodium thiododecylate. Carbon disulfide (6.0 g, 79 mmol) was then added into the slurry to generate sodium *s*-propane trithiocarbonate as a yellow precipitate, which was collected by filtration for future use.

The above prepared sodium *s*-propane trithiocarbonate (7.85 g, 49 mmol) was dissolved in diethyl ether (100 mL) and slowly added with solid iodine (6.3 g, 25 mmol). After the reaction mixture was stirred at room temperature for 1 h, sodium iodide as a white solid was produced and removed by filtration. The yellow-brown filtrate was washed with the sodium thiosulfate solution to remove excess iodine, washed with water, dried with sodium sulfate, and evaporated by the rotary evaporator to obtain bis(propane sulfanylthiocarbonyl) disulfide for future use.

A mixture of 4,4-azobis(4-cyanopentanoic acid) (4.339 g, 1.5 mmol) and the above prepared bis(propane sulfanylthiocarbonyl) disulfide (6.5 g, 1 mmol) was refluxed in dry ethyl acetate (150 mL) for 18 h under N_2 protection. The reaction mixture was then extracted with water, dried with sodium sulfate, and evaporated by the rotary evaporator to get the crude product. After purification by silica gel column chromatography with petroleum ether and ethyl acetate (v/v,

https://doi.org/10.1021/acsami.1c00842
ACS Appl. Mater. Interfaces 2021, 13, 14951−14963

1:1) as the eluent, the RAFT agent ECT was obtained as a pale yellow solid (8.34 g, 77% yield). ^{1}H NMR ($CDCl_3$, 400 MHz, 298 K) δ (ppm): 3.30 (t, 2H, $-CH_2S$, J = 7.13 Hz), 2.66 (dd, 2H, $-CH_2COO$, J_1 = 8.11 Hz, J_2 = 9.05 Hz), 2.54 (m, 1H, −CHHCCN), 2.41 (m, 1H, −CHHCCN), 1.88(s, 3H, $-CH_3$), 1.75 (m, 2H, $-CH_2CH_3$), 1.02 (t, 3H, $-CH_2CH_3$, J = 7.35 Hz) (Figure S1b).

Synthesis of NBOC. 2-Nitrobenzyl alcohol (1 g, 6.53 mmol) and 2-isocyanatoethyl methacrylate (1.52 g, 9.8 mmol) were dissolved in anhydrous THF (20 mL) in a Schlenk flask under N_2 protection with the addition of the catalytic amount DBTL (50 μL). The mixture was stirred overnight at room temperature, and the reaction process was monitored by thin-layer chromatography (TLC) until completion. After removing the solvent under reduced pressure, the as-obtained crude product was dissolved in dichloromethane, washed with saturated NaCl solution, dried by $MgSO_4$, and concentrated under reduced pressure. After further purification by silica gel column chromatography with dichloromethane and ethyl acetate (v/v, 10:1) as the eluent, 2-nitrobenzyloxycarbonylaminoethylmethacrylate (NBOC) was obtained as a yellow solid (2.34 g, 93% yield). ^{1}H NMR (CD_3OD, 400 MHz, 298 K) δ (ppm): 8.12 (d, 1H, Ar-H, J = 7.54 Hz), 7.67 (m, 2H, Ar-H), 7.54 (t, 1H, Ar-H, J = 8.04 Hz), 6.11 (s, 1H, −CCHH), 5.61 (s, 1H, −CCHH), 5.45 (s, 2H, Ar-CH_2−), 4.21 (t, 2H, $-CH_2COO-$, J = 5.50 Hz), 3.44 (t, 2H, $-NHCH_2-$, J = 5.14 Hz), 1.92 (s, 3H, $-CH_3$) (Figure S1c).

Synthesis of GA-NH_2. Glycyrrhetinic acid (GA, 470.64 mg, 3 mmol) and *N*-hydroxysuccinimide (NHS, 115.09 mg, 3.6 mmol) were dissolved in dry dichloromethane (50 mL) in a Schlenk flask under N_2 protection with the subsequent addition of *N*-dicyclohexylcarbodiimide (DCC, 206.33 mg, 3.6 mmol) at 0 °C. After being stirred overnight at room temperature, the reaction mixture was filtered to remove dicylcohexylurea as the byproduct during the reaction process. The filtrate was then collected, drop-wise added with ethylenediamine (5 mL), and stirred at room temperature for 24 h. After removing the solvent with rotary evaporator, the remaining solid was dissolved in DMF (5 mL) and poured into distilled water under stirring, and the as-obtained precipitate was dried in vacuum at 60 °C to obtain GA-NH_2 as a white solid (370 mg, 79% yield).

Synthesis of the Hydrophilic Block *P*(OEGMA$_{0.98}$-*co*-EoS$_{0.02}$)$_{11}$ and Diblock Copolymer *P*(OEGMA$_{0.98}$-*co*-EoS$_{0.02}$)$_{11}$-*b*-PNBOC via RAFT Polymerization. *P*(OEGMA-*co*-EoS) was prepared via reversible addition−fragmentation chain transfer (RAFT) polymerization. OEGMA (2.02 g, 4.04 mmol), derived EoS (61.43 mg, 0.08 mmol), ECT (57.15 mg, 0.206 mmol), and AIBN (3.38 mg, 0.0206 mmol) were dissolved in 1,4-dioxane (1.4 mL). The reaction tube was carefully degassed by three freeze−pump−thaw cycles and sealed under N_2. After stirring for 5 h at 70 °C, the reaction tube was quenched with liquid nitrogen, exposed to air, and added with excess diethyl ether for precipitation. The obtained precipitate was re-dissolved with a small amount of dichloromethane and precipitated with excess diethyl ether, and the cycle was repeated thrice. After being dried in a vacuum oven overnight at room temperature, *P*(OEGMA-*co*-EoS) was obtained as a red solid (1.28 g, 60% yield) (Figure S2a). The molecular weight and molecular weight distribution of *P*(OEGMA-*co*-EoS) were determined by GPC using DMF as the eluent, revealing an M_n (average molecular weight) of 5 kDa and M_w/M_n (molecular weight distribution) of 1.18. The degree of polymerization (DP) of *P*(OEGMA-*co*-EoS) was determined to be ∼11 by ^{1}H NMR spectroscopy (Figure S2a). The molar content of the derived EoS moiety was determined to be 2% by ^{1}H NMR spectroscopy (Figure S2a). Thus, the as-synthesized polymer was denoted as *P*(OEGMA$_{0.98}$-*co*-EoS$_{0.02}$)$_{11}$.

To prepare *P*(OEGMA$_{0.98}$-*co*-EoS$_{0.02}$)$_{11}$-*b*-PNBOC, the above obtained *P*(OEGMA$_{0.98}$-*co*-EoS$_{0.02}$)$_{11}$ (288 mg, 0.05 mmol) was mixed with NBOC (616 mg, 2 mmol) and AIBN (1.6 mg, 0.01 mmol) and dissolved with 1,4-dioxane (1.3 mL) in a reaction tube with a magnetic stirring bar. The reaction tube was degassed by three freeze−pump−thaw cycles and sealed under N_2. After stirring at 70 °C for 24 h, the reaction tube was quenched with liquid nitrogen, exposed to air, and added with excess of diethyl ether for precipitation. The obtained precipitate was re-dissolved into dichloromethane (2 mL) and re-precipitated with diethyl ether (200 mL), and the process was repeated thrice (Figure S2b). After being dried under vacuum, *P*(OEGMA$_{0.98}$-*co*-EoS$_{0.02}$)$_{11}$-*b*-PNBOC was obtained as a red solid (0.5 g, 56% yield). The molecular weight and molecular weight distribution were determined to be 10.6 and 1.10 by GPC using DMF as the eluent, respectively, and the degree of polymerization (DP) was determined by ^{1}H NMR analysis. By adjusting the NBOC amount, the DP of PNBOC was adjusted among 18, 37, 46, and 53 (Table S1).

GA-NH_2 was conjugated to the main chain of the above obtained *P*(OEGMA$_{0.98}$-*co*-EoS$_{0.02}$)$_{11}$-*b*-PNBOC$_{46}$ diblock copolymer via amide reaction. Briefly, *P*(OEGMA$_{0.98}$-*co*-EoS$_{0.02}$)$_{11}$-*b*-PNBOC$_{46}$ (80 mg) was dissolved in THF solution (10 mL), and EDC (20.7 mg, 0.108 mmol)/NHS (10.36 mg, 0.09 mmol) was added to activate the carboxyl group of *P*(OEGMA$_{0.98}$-*co*-EoS$_{0.02}$)$_{11}$-*b*-PNBOC$_{46}$. After reaction for 4 h at room temperature, the GA-NH_2 (25 mg) was added to the above reaction mixture and continuously reacted for 18 h. The mixture was precipitated in excess cold diethyl ether, and the precipitate was washed two times with cold diethyl ether to remove excess GA-NH_2. The as-obtained precipitate was dried in vacuum at 40 °C to obtain GA-conjugated *P*(OEGMA$_{0.98}$-*co*-EoS$_{0.02}$)$_{11}$-*b*-PNBOC$_{46}$.

Synthesis of PEG-Stabilized UCNPs (UCNPs-PEG). Upconversion nanoparticles $NaYF_4$:Yb,Gd,Tm,Er (UCNPs) were synthesized according to a previously reported method with a small modification.[47] In brief, YCl_3 (132.78 mg, 0.68 mmol), $GdCl_3$ (26.37 mg, 0.1 mmol), $YbCl_3$ (54.68 mg, 0.2 mmol), $TmCl_3$ (5.51 mg, 0.02 mmol), and $ErCl_3$ (0.55 mg, 0.002 mmol) were added into a mixture of oleic acid (8 mL) and 1-octadecene (15 mL), heated to 160 °C under vacuum, and stirred for 60 min to remove water and oxygen, which resulted in a clear solution. After cooling down to room temperature, the methanol solution (10 mL) of NH_4F (148 mg, 4.0 mmol) and NaOH (100 mg, 2.5 mmol) was added wisely into the mixture under stirring for 30 min. The reaction mixture was heated to 90 °C for 15 min and 325 °C under a nitrogen atmosphere. The reaction progress was monitored by the upconversion luminescence measurement, and the reaction mixture was cooled down to room temperature when the upconversion luminescence appeared. The as-obtained UCNPs were precipitated with excess ethanol, centrifuged at 12,000 g for 5 min, repeatedly washed with ethanol, and re-dispersed in 10 mL of cyclohexane for further use.

PEG-phosphate (PEG-POOH) was synthesized according to a previously reported method with a small optimization[48] and used as a stabilizing ligand for UCNPs. Briefly, phosphoryl trichloride ($POCl_3$, 2.127 g, 13.87 mmol) was added into anhydrous THF (10 mL) under a flowing N_2 atmosphere and mixed with anhydrous THF (30 mL)-dissolved mPEG (5.08 g, 9.25 mmol), and the reaction mixture was heated to 55 °C under flowing N_2 to remove the byproduct HCl. After reaction for 6 h, the reaction mixture was subsequently cooled to room temperature, added with cold water (5 mL), and continuously stirred for 1 h at room temperature. THF was then removed via rotary evaporation, and the aqueous solution was lyophilized to obtain PEG-POOH. PEG-stabilized UCNPs (PEG-UCNPs) were prepared according to a previously reported method.[49] The above prepared UCNPs (5 mg/mL) was dispersed in cyclohexane (5 mL) and mixed with a DMF (5 mL) solution of $NOBF_4$ (0.01 M) at room temperature, shaken gently for 30 min, centrifuged, and re-dispersed in DMF. Subsequently, PEG-POOH (80 mg) was added into the above obtained DMF-dispersed UCNP solution (10 mL, 2.5 mg/mL), heated to 75 °C, and vigorously stirred for 12 h to get PEG-UCNPs.

Self-Assembly of the Biomimetic Polymersome and Encapsulation of AQ4N and PEG-UCNPs. The above prepared *P*(OEGMA-*co*-EoS)-*b*-PNBOC with different hydrophobic block DP values from 18 to 53 were self-assembled, respectively, into various morphologies in an aqueous solution (Table S1, P1−P4). The block copolymer (2 mg) was dissolved in THF (1 mL) and stirred at 25 °C for 30 min. Water (1 mL) was subsequently added slowly to the THF solution within 1 h, which was followed by the injection of 7 mL of

https://doi.org/10.1021/acsami.1c00842
ACS Appl. Mater. Interfaces 2021, 13, 14951−14963

water within 2 h. After another 4 h of stirring, THF was removed by dialysis (M_w = 3.5 kDa) against deionized water to obtain the assembly.

Hydrophilic PEG-UNCPs and AQ4N as the hypoxia-activated prodrug were encapsulated into an aqueous cavity of polymersomes $P(OEGMA_{0.98}$-*co*-$EoS_{0.02})_{11}$-*b*-$PNBOC_{46}$ (P3) during its self-assembly process. After dissolving 2 mg of diblock copolymers P3 in THF (1 mL) and maintaining stirring at 25 °C for 30 min, the AQ4N (1 mg) and PEG-UCNP (5 mg) aqueous solution (1 mL) was slowly added in within 1 h, which was followed by the injection of 7 mL of water within 2 h. After another 4 h of stirring, THF and non-encapsulated AQ4N were removed by dialysis (M_w = 3.5 kDa) against deionized water, non-encapsulated PEG-UCNPs were removed by centrifugation at 8000 g for 5 min, AQ4N- and PEG-UCNP-encapsulated polymersomes (AQ4N/PEG-UCNPs-polymersome) were obtained and characterized with the TEM image and DLS measurement. Only PEG-UCNP-encapsulated polymersomes (PEG-UCNPs-polymersomes) were prepared with the same procedure without the addition of AQ4N.

AQ4N Release from the AQ4N/PEG-UCNPs-Polymersome. *In vitro* AQ4N release from the AQ4N/PEG-UCNPs-polymersome was performed at 37 °C with a 980 nm light exposure. AQ4N/PEG-UCNPs-polymersome (10 mg) was dispersed in 10 mL of PBS (pH 7.4) and sealed in a dialysis tube (M_n = 3.5 kDa), immersed in 20 mL of PBS, and gently shaken in a shaker at 250 rpm at 37 °C. The UV−vis absorption measurement of PBS was performed at predetermined time intervals with the supplement of 20 mL of fresh PBS. The amount of cumulative AQ4N released was quantified by comparing with an AQ4N standard calibration curve ($y = 0.07 + 4.96x$, $R^2 = 0.99$, Figure S6b).

***In vitro* ROS Generation and Oxygen Consumption Rate Assay.** The ROS probe DPBF was used to detect ROS generation *in vitro*. Briefly, 4 mL of AQ4N/PEG-UCNPs-polymersome(GA) (0.25 mg/mL) was mixed with 20 μL of the DPBF ethanol solution (5 mg/mL) and irradiated with a 980 nm laser at 2 W/cm^2, and the absorbance of DPBF was recorded at 420 nm after 30 min of incubation. The same experiment was also carried out in the absence of a 980 nm laser irradiation as a control.

$[Ru(dpp)_3]Cl_2$ served as the indicator probe to measure oxygen consumption. Briefly, 150 μL of the PEG-UCNPs-polymersome(GA) (0.25 mg/mL) containing 30 μL of the DPBF (5 mg/mL) solution was placed in a 96-well plate and covered with oil. After that, the samples were exposed to a 980 nm laser with a power density of 2 W/cm^2 at different time intervals. Immediately after 20 μL of $[Ru(dpp)_3]Cl_2$ ethanol solution was added into the samples, the samples were detected by a fluorescence spectrometer with an excitation/emission wavelength of 455/600−700 nm. The PEG-UCNPs-polymersome(GA) in the absence of a 980 nm laser irradiation as a control was also measured using the same method mentioned above.

Intracellular Delivery and Mitochondrial Co-localization of AQ4N. To demonstrate the intracellular delivery specificity, HepG2 cells were incubated with the AQ4N/PEG-UCNPs-polymersome and AQ4N/PEG-UCNPs-polymersome(GA) at 37 °C for 6 h, stained with 0.1 μg/mL DAPI for 5 min, and washed with PBS twice to take the CLSM image. To further confirm the GA-assisted internalization process of the polymersome, HepG2 cells were pretreated with 2.5 mg/mL GA for 2 h, washed with PBS, then incubated with the AQ4N/PEG-UCNPs-polymersome(GA) for another 6 h before observing the CLSM image.

To visualize the co-localization of the internalized AQ4N/PEG-UCNPs-polymersome(GA) with mitochondrial compartments, HepG2 cells were incubated with the AQ4N/PEG-UCNPs-polymersome(GA) and AQ4N/PEG-UCNPs-polymersome, respectively, at 37 °C for 6 h, and mitochondrial compartments were stained with 250 nM Mito-Tracker dyes at 37 °C for 15 min to observe the CLSM images.

Intracellular ROS Generation and Hypoxia Extent Detection. An oxidative stress/hypoxia detection kit was used to demonstrate the intracellular ROS generation and hypoxia extent. The PEG-UCNPs-polymersome(GA) was incubated with HepG2 cells under a normoxic environment and hypoxic environment, respectively, for 6 h, and the culture medium was subsequently replaced with fresh DMEM containing a hypoxia and oxidative stress reagent. After being continuously cultured for 30 min, the HepG2 cells were exposed to a 980 nm laser irradiation at a power density of 2 W/cm^2 for 30 min (5 min interval for every 10 min), washed with PBS, followed by taking the green fluorescence of ROS and red fluorescence of hypoxia with CLSM. The PEG-UCNPs-polymersome-(GA) in the absence of a 980 nm laser irradiation was also measured with oxidative stress/hypoxia detection kit as a control. Moreover, flow cytometry was also performed to detect ROS/hypoxia generation efficiency. The HepG2 cells were incubated with the PEG-UCNPs-polymersome(GA) and treated with the same procedure as described above. Finally, HepG2 cells were collected by centrifugation at 800 g for 5 min, washed with PBS twice, and measured by flow cytometry over FL1 for the oxidative stress channel and FL3 for the hypoxia channel.

The duration time of an intensified hypoxic microenvironment induced by ROS generation and O_2 consumption was also studied using $[Ru(dpp)_3]Cl_2$. HepG2 cells were treated with the PEG-UCNPs-polymersome and incubated for 6 h in the incubator with 5% of O_2. After 30 min of irradiation (5 min interval for every 10 min of light exposure to avoid heating), $[Ru(dpp)_3]Cl_2$ was added, and the fluorescence images were observed by CLSM at different time intervals with the fluorescence intensity calculated by Image-Pro Plus 6.0 software.

MTT Assay. The cytotoxicity of the AQ4N/PEG-UCNPs-polymersome(GA) toward HepG2 cells was evaluated via MTT assay. HepG2 cells at a density of 1 × 10^4 cells/well were seeded in 96-well plates and incubated for 24 h. The cell culture medium was then replaced with fresh DMEM containing serial concentrations of AQ4N/PEG-UCNPs-polymersome(GA) and continuously incubated for 48 h. Then, 5 mg/mL MTT (20 μL) was added into each well subsequently and incubated for 4 h. After removing the culture medium, 80 μL of DMSO was added to dissolve the crystal precipitates, and the optical density was measured at 490 nm with a Bio-Rad microplate reader. The relative cell viability was calculated by $(A_{test}/A_{control}) \times 100\%$. HepG2 cells incubated with PBS in the absence of the AQ4N/PEG-UCNPs-polymersome(GA) served as controls.

The cell proliferation for HepG2 cells incubated with the AQ4N/PEG-UCNPs-polymersome(GA) and PEG-UCNPs-polymersome-(GA) under normoxic/hypoxic environments in the presence of NIR laser for 30 min was evaluated by MTT assay according to the same procedure as described above. The AQ4N/PEG-UCNPs-polymersome(GA) in the absence of NIR laser irradiation and PBS-treated HepG2 cells served as the control. To demonstrate the contribution of AQ4N sustained release, the mixture of free AQ4N and PEG-UCNPs-polymersome(GA)-treated HepG2 cells was also irradiated with NIR light (2 W/cm^2, 30 min, 5 min interval for every 10 min) under normoxic/hypoxic environments, and the cell proliferation was measured with MTT assay.

Cell Apoptosis Assay. HepG2 cells at a density of 1 × 10^5 cells/well were seeded into a 6-well plate and incubated for 24 h. The cells were then incubated with the AQ4N/PEG-UCNPs-polymersome-(GA) and PEG-UCNPs-polymersome(GA) under normoxic/hypoxic environments, respectively, in the presence of NIR laser for 30 min. After 48 h of incubation, the cells were collected, washed with PBS twice, stained with Annexin V-FITC/propidium iodide for 15 min, and measured by flow cytometry over FL1 (Annexin V-FITC) and FL3 (PI) channels. AQ4N/PEG-UCNPs-polymersome(GA)-incubated HepG2 cells and PBS-treated HepG2 cells in the absence of NIR laser irradiation served as controls, and the mixture of free AQ4N and PEG-UCNPs-polymersome(GA)-treated HepG2 cells in the presence of NIR (2 W/cm^2, 30 min, 5 min interval for every 10 min) was also carried out to confirm the contribution of AQ4N sustained release.

Tumor Hypoxic Region and Blood Vessels Density Determination. The immunofluorescence staining was utilized to

https://doi.org/10.1021/acsami.1c00842
ACS Appl. Mater. Interfaces 2021, 13, 14951−14963

indicate the intracellular hypoxic region and decrease in blood vessel density in the tumor. HepG2 tumor-bearing mice were intratumorally injected with 80 μL of the PEG-UCNPs-polymersome(GA) (0.2 mg/mL) and irradiated with a 980 nm laser at a power density of 2 W/cm^2 for 30 min (5 min interval for every 10 min). The mice without NIR irradiation were used as controls. The mice were sacrificed 24 h post NIR irradiation, and the obtained tumor was fixed with 4% paraformaldehyde, embedded in paraffin, sliced, stained with hypoxia-inducible factor (HIF)-1a to label the tumor hypoxic regions and rat anti-mouse CD31 antibody to label blood vessels, respectively, according to the procedure provided by the manufacturers. The stained tumor slice was observed by CLSM, and the images of the hypoxic region and blood vessel density were statistically analyzed using Image-Pro Plus 6.0 software.

***In Vivo* Antitumor Efficiency.** All animal experiments were approved by the Model Animal Research Center of KeyGEN BioTECH and followed the Institutional Animal Use and Care Regulations. Specific pathogen-free female BALB/c nude mice were purchased from KeyGEN BioTECH (Nanjing, China). The tumor models were established by a subcutaneous injection of HepG2 cells with a cell concentration of 1.0×10^7 cells/mL into the selected positions of the nude mice. When the tumor volume reached 80 mm^3, the tumor-bearing mice were randomly divided into four groups and intratumorally injected with 80 μL of PBS, PEG-UCNPs-polymersome(GA), AQ4N/PEG-UCNPs-polymersome(GA) (two groups), and the mixture of free AQ4N and PEG-UCNPs-polymersome(GA) at a dose of 1.2 mmol AQ4N per mouse. The mouse groups treated with the PEG-UCNPs-polymersome(GA), AQ4N/PEG-UCNPs-polymersome(GA), and the mixture of free AQ4N and PEG-UCNPs-polymersome(GA) were irradiated with a 980 nm laser at a power density of 2 W/cm^2 for 30 min (5 min interval for every 10 min), while PBS- and AQ4N/PEG-UCNPs-polymersome(GA)-treated mouse groups without 980 nm irradiation served as controls. Both injection and irradiation were carried out at day 4 and day 8 repeatedly. The therapeutic effect was evaluated by measuring tumor volumes using a vernier caliper, and the tumor volumes were calculated as $V = (L \times W^2)/2$, in which L and W are the length and width of the tumor, respectively. In addition, the body weights of each group of mice were recorded during the therapeutic process. After 16 days of treatment, all mice were sacrificed. The obtained tumors were fixed with 4% paraformaldehyde, embedded in paraffin, sliced, stained with hematoxylin–eosin (H&E) and TUNEL, and observed by fluorescence microscopy (IX71, Olympus). Moreover, the histopathological analyses of the heart, spleen, kidney, liver, and lung at day 16 were conducted via the same method mentioned above and observed by fluorescence microscopy.

■ ASSOCIATED CONTENT

Supporting Information

The Supporting Information is available free of charge at https://pubs.acs.org/doi/10.1021/acsami.1c00842.

Materials and apparatus, cell culture, synthetic routes of the monomer and block copolymer, ^{1}H NMR spectra of the monomer and block copolymer, structural parameters of $P(OEGMA_{0.98}\text{-co-}EoS_{0.02})_{11}\text{-}b\text{-}PNBOC_n$, DLS analysis, TEM images, UV–vis spectra, confocal fluorescence images, relative cell viabilities, flow cytometry analysis, tumor weight, body weight, and H&E staining images (PDF)

■ AUTHOR INFORMATION

Corresponding Author

Ying Liu − *State Key Laboratory of Analytical Chemistry for Life Science, School of Chemistry and Chemical Engineering and Chemistry and Biomedicine Innovation Center, Nanjing University, Nanjing 210023, China;* orcid.org/0000-0001-5718-7804; Email: yingliu@nju.edu.cn

Authors

Yuling He − *State Key Laboratory of Analytical Chemistry for Life Science, School of Chemistry and Chemical Engineering, Nanjing University, Nanjing 210023, China*

Shuwen Guo − *State Key Laboratory of Quality Research in Chinese Medic, Institute of Chinese Medical Sciences, University of Macau, Macao 999078, China*

Yue Zhang − *State Key Laboratory of Analytical Chemistry for Life Science, School of Chemistry and Chemical Engineering, Nanjing University, Nanjing 210023, China;* orcid.org/0000-0002-7902-4253

Huangxian Ju − *State Key Laboratory of Analytical Chemistry for Life Science, School of Chemistry and Chemical Engineering, Nanjing University, Nanjing 210023, China;* orcid.org/0000-0002-6741-5302

Complete contact information is available at: https://pubs.acs.org/10.1021/acsami.1c00842

Author Contributions

Y.H. and S.G. contributed equally to this work.

Notes

The authors declare no competing financial interest.

■ ACKNOWLEDGMENTS

We gratefully acknowledge the National Natural Science Foundation of China (21974064, 22022405, and 21635005), Natural Science Foundation of Jiangsu Province for distinguished Young Scholars (BK20200010), Specially-Appointed Professor Foundation of Jiangsu Province, Program for Innovative Talents and Entrepreneurs of Jiangsu Province, State Key Laboratory of Analytical Chemistry for Life Science (5431ZZXM2003), and Fundamental Research Funds for the Central Universities (14380472).

■ REFERENCES

(1) Lu, Y.; de Vries, W. C.; Overeem, N. J.; Duan, X.; Zhang, H.; Zhang, H.; Pang, W.; Ravoo, B. J.; Huskens, J. Controlled and Tunable Loading and Release of Vesicles by Using Gigahertz Acoustics. *Angew. Chem., Int. Ed.* **2019**, *58*, 159–163.

(2) Chiu, H.-C.; Lin, Y.-W.; Huang, Y.-F.; Chuang, C.-K.; Chern, C.-S. Polymer Vesicles Containing Small Vesicles within Interior Aqueous Compartments and pH-responsive Transmembrane Channels. *Angew. Chem., Int. Ed.* **2008**, *47*, 1875–1878.

(3) Antonietti, M.; Förster, S. Vesicles and Liposomes: A Self-Assembly Principle Beyond Lipids. *Adv. Mater.* **2003**, *15*, 1323–1333.

(4) Edlinger, C.; Einfalt, T.; Spulber, M.; Car, A.; Meier, W.; Palivan, C. G. Biomimetic Strategy to Reversibly Trigger Functionality of Catalytic Nanocompartments by the Insertion of pH-Responsive Biovalves. *Nano Lett.* **2017**, *17*, 5790–5798.

(5) Einfalt, T.; Goers, R.; Dinu, I. A.; Najer, A.; Spulber, M.; Onaca-Fischer, O.; Palivan, C. G. Stimuli-Triggered Activity of Nanoreactors by Biomimetic Engineering Polymer Membranes. *Nano Lett.* **2015**, *15*, 7596–7603.

(6) Liu, C.; Li, C.; Pang, C.; Li, M.; Li, H.; Li, P.; Fan, L.; Liu, H.; Tian, W. Supramolecular Drug–Drug Complex Vesicles Enable Sequential Drug Release for Enhanced Combination Therapy. *ACS Appl. Mater. Interfaces* **2020**, *12*, 27940–27950.

(7) Messager, L.; Burns, J. R.; Kim, J.; Cecchin, D.; Hindley, J.; Pyne, A. L. B.; Gaitzsch, J.; Battaglia, G.; Howorka, S. Biomimetic Hybrid Nanocontainers with Selective Permeability. *Angew. Chem., Int. Ed.* **2016**, *55*, 11106–11109.

(8) Wilson, D. A.; Nolte, R. J. M.; van Hest, J. C. M. Autonomous Movement of Platinum-Loaded Stomatocytes. *Nat. Chem.* **2012**, *4*, 268–274.

(9) Palivan, C. G.; Goers, R.; Najer, A.; Zhang, X.; Car, A.; Meier, W. Bioinspired Polymer Vesicles and Membranes for Biological and Medical Applications. *Chem. Soc. Rev.* **2016**, *45*, 377−411.
(10) Einfalt, T.; Witzigmann, D.; Edlinger, C.; Sieber, S.; Goers, R.; Najer, A.; Spulber, M.; Onaca-Fischer, O.; Huwyler, J.; Palivan, C. G. Biomimetic Artificial Organelles with *In Vitro* and *In Vivo* Activity Triggered by Reduction in Microenvironment. *Nat. Commun.* **2018**, *9*, 1127.
(11) Liu, Y.; Yang, Z.; Huang, X.; Yu, G.; Wang, S.; Zhou, Z.; Shen, Z.; Fan, W.; Liu, Y.; Davisson, M.; Kalish, H.; Niu, G.; Nie, Z.; Chen, X. Glutathione-Responsive Self-Assembled Magnetic Gold Nanowreath for Enhanced Tumor Imaging and Imaging-Guided Photothermal Therapy. *ACS Nano* **2018**, *12*, 8129−8137.
(12) Zhu, R.; Su, L.; Dai, J.; Li, Z.-W.; Bai, S.; Li, Q.; Chen, X.; Song, J.; Yang, H. Biologically Responsive Plasmonic Assemblies for Second Near-Infrared Window Photoacoustic Imaging-Guided Concurrent Chemo-Immunotherapy. *ACS Nano* **2020**, *14*, 3991−4006.
(13) Liu, X.; Appelhans, D.; Voit, B. Hollow Capsules with Multiresponsive Valves for Controlled Enzymatic Reactions. *J. Am. Chem. Soc.* **2018**, *140*, 16106−16114.
(14) Deng, Z.; Qian, Y.; Yu, Y.; Liu, G.; Hu, J.; Zhang, G.; Liu, S. Engineering Intracellular Delivery Nanocarriers and Nanoreactors from Oxidation-Responsive Polymersomes via Synchronized Bilayer Cross-Linking and Permeabilizing Inside Live Cells. *J. Am. Chem. Soc.* **2016**, *138*, 10452−10466.
(15) Fischer, A.; Lilienthal, S.; Vázquez-González, M.; Fadeev, M.; Sohn, Y. S.; Nechushtai, R.; Willner, I. Triggered Release of Loads from Microcapsule-in-Microcapsule Hydrogel Microcarriers: En-Route to an "Artificial Pancreas". *J. Am. Chem. Soc.* **2020**, *142*, 4223−4234.
(16) Deng, Z.; Yuan, S.; Xu, R. X.; Liang, H.; Liu, S. Reduction-Triggered Transformation of Disulfide-Containing Micelles at Chemically Tunable Rates. *Angew. Chem., Int. Ed.* **2018**, *57*, 8896−8900.
(17) Zhao, T.; Wang, P.; Li, Q.; Al-Khalaf, A. A.; Hozzein, W. N.; Zhang, F.; Li, X.; Zhao, D. Near-Infrared Triggered Decomposition of Nanocapsules with High Tumor Accumulation and Stimuli Responsive Fast Elimination. *Angew. Chem., Int. Ed.* **2018**, *57*, 2611−2615.
(18) Deng, H.; Lin, L.; Wang, S.; Yu, G.; Zhou, Z.; Liu, Y.; Niu, G.; Song, J.; Chen, X. X-ray-Controlled Bilayer Permeability of Bionic Nanocapsules Stabilized by Nucleobase Pairing Interactions for Pulsatile Drug Delivery. *Adv. Mater.* **2019**, *31*, 1903443.
(19) Yao, C.; Wang, P.; Li, X.; Hu, X.; Hou, J.; Wang, L.; Zhang, F. Near-Infrared-Triggered Azobenzene-Liposome/Upconversion Nanoparticle Hybrid Vesicles for Remotely Controlled Drug Delivery to Overcome Cancer Multidrug Resistance. *Adv. Mater.* **2016**, *28*, 9341−9348.
(20) Deng, Z.; Wang, N.; Liu, Y.; Xu, Z.; Wang, Z.; Lau, T.-C.; Zhu, G. A Photocaged, Water-Oxidizing, and Nucleolus-Targeted Pt(IV) Complex with a Distinct Anticancer Mechanism. *J. Am. Chem. Soc.* **2020**, *142*, 7803−7812.
(21) Mou, Q.; Ma, Y.; Ding, F.; Gao, X.; Yan, D.; Zhu, X.; Zhang, C. Two-in-One Chemogene Assembled from Drug-Integrated Antisense Oligonucleotides to Reverse Chemoresistance. *J. Am. Chem. Soc.* **2019**, *141*, 6955−6966.
(22) Pusuluri, A.; Krishnan, V.; Lensch, V.; Sarode, A.; Bunyan, E.; Vogus, D. R.; Menegatti, S.; Soh, H. T.; Mitragotri, S. Treating Tumors at Low Drug Doses Using an Aptamer-Peptide Synergistic Drug Conjugate. *Angew. Chem., Int. Ed.* **2019**, *58*, 1437−1441.
(23) Kenaan, A.; Cheng, J.; Qi, D.; Chen, D.; Cui, D.; Song, J. Physicochemical Analysis of DPPC and Photopolymerizable Liposomal Binary Mixture for Spatiotemporal Drug Release. *Anal. Chem.* **2018**, *90*, 9487−9494.
(24) Qiu, M.; Wang, D.; Liang, W.; Liu, L.; Zhang, Y.; Chen, X.; Sang, D. K.; Xing, C.; Li, Z.; Dong, B.; Xing, F.; Fan, D.; Bao, S.; Zhang, H.; Cao, Y. Novel Concept of the Smart NIR-light-Controlled Drug Release of Black Phosphorus Nanostructure for Cancer Therapy. *Proc. Natl. Acad. Sci.* **2018**, *115*, 501−506.
(25) Zhang, Y.; Tsitkov, S.; Hess, H. Complex Dynamics in a Two-Enzyme Reaction Network with Substrate Competition. *Nat. Catal.* **2018**, *1*, 276−281.
(26) Che, H.; Cao, S.; van Hest, J. C. M. Feedback-Induced Temporal Control of "Breathing" Polymersomes to Create Self-Adaptive Nanoreactors. *J. Am. Chem. Soc.* **2018**, *140*, 5356−5359.
(27) Yang, M.; Chan, H.; Zhao, G.; Bahng, J. H.; Zhang, P.; Král, P.; Kotov, N. A. Self-Assembly of Nanoparticles into Biomimetic Capsid-Like Nanoshells. *Nat. Chem.* **2017**, *9*, 287−294.
(28) Wang, Y.; Deng, Y.; Luo, H.; Zhu, A.; Ke, H.; Yang, H.; Chen, H. Light-Responsive Nanoparticles for Highly Efficient Cytoplasmic Delivery of Anticancer Agents. *ACS Nano* **2017**, *11*, 12134−12144.
(29) Cheng, Q.; Duan, H.; Hao, A.; Xing, P. Photoregulated "Breathing" Vesicle with Inversed Supramolecular Chirality. *ACS Appl. Mater. Interfaces* **2021**, *13*, 2091−2099.
(30) Lee, J.; Ku, K. H.; Kim, J.; Lee, Y. J.; Jang, S. G.; Kim, B. J. Light-Responsive, Shape-Switchable Block Copolymer Particles. *J. Am. Chem. Soc.* **2019**, *141*, 15348−15355.
(31) Li, S.; Xia, B.; Javed, B.; Hasley, W. D.; Melendez-Davila, A.; Liu, M.; Kerzner, M.; Agarwal, S.; Xiao, Q.; Torre, P.; Bermudez, J. G.; Rahimi, K.; Kostina, N. Y.; Möller, M.; Rodriguez-Emmenegger, C.; Klein, M. L.; Percec, V.; Good, M. C. Direct Visualization of Vesicle Disassembly and Reassembly Using Photocleavable Dendrimers Elucidates Cargo Release Mechanisms. *ACS Nano* **2020**, *14*, 7398−7411.
(32) Yi, Q.; Sukhorukov, G. B. Externally Triggered Dual Function of Complex Microcapsules. *ACS Nano* **2013**, *7*, 8693−8705.
(33) Huang, F.; Liao, W.-C.; Sohn, Y. S.; Nechushtai, R.; Lu, C.-H.; Willner, I. Light-Responsive and pH-Responsive DNA Microcapsules for Controlled Release of Loads. *J. Am. Chem. Soc.* **2016**, *138*, 8936−8945.
(34) Chen, H.; Xiao, L.; Anraku, Y.; Mi, P.; Liu, X.; Cabral, H.; Inoue, A.; Nomoto, T.; Kishimura, A.; Nishiyama, N.; Kataoka, K. Polyion Complex Vesicles for Photoinduced Intracellular Delivery of Amphiphilic Photosensitizer. *J. Am. Chem. Soc.* **2014**, *136*, 157−163.
(35) Rifaie-Graham, O.; Ulrich, S.; Galensowske, N. F. B.; Balog, S.; Chami, M.; Rentsch, D.; Hemmer, J. R.; Read de Alaniz, J.; Boesel, L. F.; Bruns, N. Wavelength-Selective Light-Responsive DASA-Functionalized Polymersome Nanoreactors. *J. Am. Chem. Soc.* **2018**, *140*, 8027−8036.
(36) He, Y.; Guo, S.; Wu, L.; Chen, P.; Wang, L.; Liu, Y.; Ju, H. Near-Infrared Boosted ROS Responsive siRNA Delivery and Cancer Therapy with Sequentially Peeled Upconversion Nano-Onions. *Biomaterials* **2019**, *225*, 119501.
(37) Zhang, Y.; Zhang, Y.; Song, G.; He, Y.; Zhang, X.; Liu, Y.; Ju, H. A DNA-Azobenzene Nanopump Fueled by Upconversion Luminescence for Controllable Intracellular Drug Release. *Angew. Chem., Int. Ed.* **2019**, *58*, 18207−18211.
(38) Moad, G.; Chong, Y. K.; Postma, A.; Rizzardo, E.; Thang, S. H. Advances in RAFT Polymerization: The Synthesis of Polymers with Defined End-Groups. *Polymer* **2005**, *46*, 8458−8468.
(39) Sun, Q.; Zhou, Z.; Qiu, N.; Shen, Y. Rational Design of Cancer Nanomedicine: Nanoproperty Integration and Synchronization. *Adv. Mater.* **2017**, *29*, 1606628.
(40) Chen, G.; Jaskula-Sztul, R.; Esquibel, C. R.; Lou, I.; Zheng, Q.; Dammalapati, A.; Harrison, A.; Eliceiri, K. W.; Tang, W.; Chen, H.; Gong, S. Neuroendocrine Tumor-Targeted Upconversion Nanoparticle-Based Micelles for Simultaneous NIR-Controlled Combination Chemotherapy and Photodynamic Therapy, and Fluorescence Imaging. *Adv. Funct. Mater.* **2017**, *27*, 1604671.
(41) Wang, X.; Hu, J.; Liu, G.; Tian, J.; Wang, H.; Gong, M.; Liu, S. Reversibly Switching Bilayer Permeability and Release Modules of Photochromic Polymersomes Stabilized by Cooperative Noncovalent Interactions. *J. Am. Chem. Soc.* **2015**, *137*, 15262−15275.
(42) Feng, L.; Cheng, L.; Dong, Z.; Tao, D.; Barnhart, T. E.; Cai, W.; Chen, M.; Liu, Z. Theranostic Liposomes with Hypoxia-Activated Prodrug to Effectively Destruct Hypoxic Tumors Post-Photodynamic Therapy. *ACS Nano* **2017**, *11*, 927−937.

https://doi.org/10.1021/acsami.1c00842
ACS Appl. Mater. Interfaces 2021, 13, 14951−14963

(43) Cao, C.; Chen, F.; Garvey, C. J.; Stenzel, M. H. Drug-Directed Morphology Changes in Polymerization-Induced Self-Assembly (PISA) Influence the Biological Behavior of Nanoparticles. *ACS Appl. Mater. Interfaces* **2020**, *12*, 30221−30233.
(44) Qian, C.; Yu, J.; Chen, Y.; Hu, Q.; Xiao, X.; Sun, W.; Wang, C.; Feng, P.; Shen, Q.-D.; Gu, Z. Light-Activated Hypoxia-Responsive Nanocarriers for Enhanced Anticancer Therapy. *Adv. Mater.* **2016**, *28*, 3313−3320.
(45) Zhang, C.; Liu, Z.; Zheng, Y.; Geng, Y.; Han, C.; Shi, Y.; Sun, H.; Zhang, C.; Chen, Y.; Zhang, L.; Guo, Q.; Yang, L.; Zhou, X.; Kong, L. Glycyrrhetinic Acid Functionalized Graphene Oxide for Mitochondria Targeting and Cancer Treatment *In Vivo*. *Small* **2018**, *14*, 1703306.
(46) Wang, W.; Moriyama, L. T.; Bagnato, V. S. Photodynamic Therapy Induced Vascular Damage: An Overview of Experimental PDT. *Laser. Phys. Lett.* **2013**, *10*, No. 023001.
(47) Dolmans, D. E. J. G. J.; Fukumura, D.; Jain, R. K. Photodynamic Therapy for Cancer. *Nat. Rev. Cancer* **2003**, *3*, 380−387.
(48) Imokawa, G.; Tsutsumi, H.; Kurosaki, T. Surface Activity and Cutaneous Effects of Monoalkyl Phosphate Surfactants. *J. Am. Oil Chem. Soc.* **1978**, *55*, 839−843.
(49) Boyer, J. C.; Manseau, M.-P.; Murray, J. I.; van Veggel, F. C. J. M. Surface Modification of Upconverting $NaYF_4$ Nanoparticles with PEG-Phosphate Ligands for NIR (800 nm) Biolabeling within the Biological Window. *Langmuir* **2010**, *26*, 1157−1164.

https://doi.org/10.1021/acsami.1c00842
ACS Appl. Mater. Interfaces 2021, 13, 14951−14963